Research Article Vol. 35, No. 6 / June 2018 / Journal of the Optical Society of America B 1475

Journal of the Optical Society of America B

OPTICAL PHYSICS

High-dielectric constant enhanced photon–exciton coupling in an evanescent vacuum

Juanjuan Ren,[1] He Hao,[1] Zhiyuan Qian,[1] Xueke Duan,[1] Fan Zhang,[1] Tiancai Zhang,[2,3] Qihuang Gong,[1,2] and Ying Gu[1,2,*]

[1]State Key Laboratory for Mesoscopic Physics, Collaborative Innovation Center of Quantum Matter, Department of Physics, Peking University, Beijing 100871, China

[2]Collaborative Innovation Center of Extreme Optics, Shanxi University, Taiyuan, Shanxi 030006, China

[3]State Key Laboratory of Quantum Optics and Quantum Optics Devices, Institute of Opto-Electronics, Shanxi University, Taiyuan 030006, China

*Corresponding author: ygu@pku.edu.cn

Received 22 February 2018; revised 1 May 2018; accepted 7 May 2018; posted 9 May 2018 (Doc. ID 324710); published 1 June 2018

Electromagnetic vacuum engineering in nanostructures can be used to tailor the light–emitter interaction at the subwavelength scale. Here, by embedding a nanocavity quantum electrodynamic system in an evanescent vacuum, we theoretically investigate high-dielectric constant enhanced photon–exciton coupling. The evanescent depth decreases as the dielectric constant of the embedding medium increases. Thus, more confined evanescent fields are obtained owing to faster exponential decay of an evanescent wave, which is used to obtain a larger coupling coefficient enhancement. The enhanced coupling coefficients are also demonstrated by changing the Ag nanorod size and the gap distance between the nanoparticle and plate. To significantly enhance the absolute value of the coupling coefficients, the Ag cylindrical nanorod can be replaced by the Ag pyramid or bipyramid. Evanescent vacuum induced strong photon–exciton coupling would have a significant influence on the fundamental physics of the subwavelength-confined cavity quantum electrodynamics and on-chip quantum information processing and scalable quantum networks.

OCIS codes: (270.0270) Quantum optics; (270.5580) Quantum electrodynamics; (240.6680) Surface plasmons.

https://doi.org/10.1364/JOSAB.35.001475

1. INTRODUCTION

Traditional cavity quantum electrodynamic (CQED) systems, which provide a quantum interface for coherent control of light–matter interaction, achieved great success in quantum information processing [1–4]. In the strong coupling regime of CQED systems, energy can be reversibly and controllably exchanged between the emitter and the cavity, where CQED systems can be used as quantum nodes for information swapping and quantum state storing [4]. To meet the requirements of on-chip quantum devices, plasmon-based CQED systems with a strongly localized field were developed extensively [5–14]. Specifically, strong coupling between emitters and metallic nanostructures was not only theoretically studied extensively [15–21] but also implemented experimentally [22–27], accompanied by energy anti-crossing and Rabi splitting. However, strong coupling between a single emitter and an individual plasmon nanostructure, which is of great significance to on-chip quantum information processing, has been rarely experimentally realized owing to ineluctable metallic loss [28–30].

Taking advantage of special modes of nanophotonic structures to obtain a custom-tailored vacuum, electromagnetic vacuum engineering is an effective solution to enhance light–matter interaction in quantum optics and cavity quantum electrodynamics. An evanescent vacuum (EV) is a specific vacuum caused by evanescent optical modes of nanophotonic structures, such as one-dimensional (1D) EV provided by metallic or dielectric nanowires [16] and the two-dimensional (2D) EV provided by a metallic nanofilm or plate. A more confined evanescent field will in principle be beneficial to obtain the larger coupling coefficient enhancement. One way to obtain a more confined field is to increase the dielectric constant of the embedding medium. It is well-known that, at the evanescent depth L_{depth} in the medium along the y direction (perpendicular to the metal-dielectric surface) (Fig. 1), the field falls to $1/e$ of the maximum value. The evanescent depth can be expressed by $L_{\mathrm{depth}} = 1/|k_y| = 1/|\sqrt{\varepsilon_b k_0^2 - k_z^2}|$, where $k_0 = 2\pi/\lambda = \omega/c$ is the wave vector in free vacuum, k_y is the wave vector along the y axis, and k_z is the wave vector along the propagation direction (z axis) [31]. Thus, with permittivity ε_b increases, the evanescent depth decreases, leading to a more localized evanescent field because of faster exponential decay of the evanescent wave. However, in the strong coupling regime, changing the permittivity of the embedding medium to enhance light–matter interaction was not investigated.

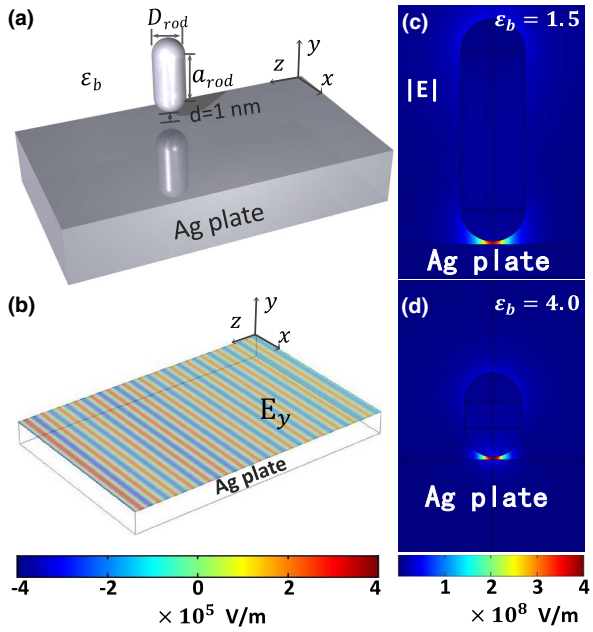

Fig. 1. (a) Diagram of a nano-CQED system in 2D EV provided by the Ag plate. (b) Evanescent optical field distribution of the Ag plate when the permittivity $\varepsilon_b = 4.0$. Electric field distributions of the longitudinal modes of the AgNR for (c) $\varepsilon_b = 1.5$ with $D_{\text{rod}} = 20$ nm and $a_{\text{rod}} = 49.6$ nm, and (d) $\varepsilon_b = 4.0$ with $D_{\text{rod}} = 20$ nm and $a_{\text{rod}} = 9.6$ nm at the wavelength $\lambda = 780$ nm.

To this end, we change the dielectric constant of the embedding medium to enhance strong photon–exciton coupling. When the permittivity of the medium above the Ag plate increases, the evanescent depth in the medium decreases. The enhancement of the coupling coefficient for a single emitter to an Ag nanorod (AgNR) at the nanogap increases relative to that in homogeneous vacuum. The main reason is due to the more confined evanescent field within the smaller evanescent depth owing to faster exponential decay. By fixing the permittivity of the medium $\varepsilon_b = 2.13$, more enhancement of the coupling coefficients for longer AgNR is obtained. Replacing the AgNR by an Ag pyramid or bipyramid, the significantly enhanced absolute value of the coupling coefficients can be obtained owing to the strongly localized field close to the nanotip, but the coupling coefficients' enhancement in EV relative to the free vacuum is small. Both exchanging energy reversibly between the plasmon nanocavity and a single emitter and Rabi splitting in the fluorescence spectra indicate that strong photon–exciton coupling appears. Achieving strong coupling in 2D EV has a major impact on the fundamental physics of nano-CQED systems and has potential applications in on-chip quantum information processing. Furthermore, the broad region of the 2D evanescent field makes embedding multi-nano-CQED systems in the same EV experimentally possible, which could be utilized in scalable quantum networks.

This paper is organized as follows: In Section 2, we set up the model of a nano-CQED system embedded in the 2D EV. Section 3 presents high-dielectric constant enhanced photon–exciton coupling. In Section 4, the coupling coefficients enhanced by changing the size of the Ag nanoparticle, size of the gap distance, and shape of the nanoparticle are demonstrated. Section 5 describes the reversible interaction between a single emitter and a single plasmon nanocavity. Finally, discussion about the experimental realization and a summary are presented.

2. MODEL SETUP

A nano-CQED system is embedded in EV [Fig. 1(a)], where an Ag nanoparticle is vertically placed close to an Ag plate, and a single emitter can be located at the nanogap. The Ag nanoparticle is too small to affect the evanescent optical mode of the plate. They are decoupled, and there is no peak splitting in the absorption spectrum of the Ag nanoparticle. Moreover, the coupling of the emitter to the nanoparticle is much stronger than that to the plate. Thus, the evanescent mode is seen as the electromagnetic background of the nano-CQED system, the so-called EV [16], and the Ag nanoparticle as the open plasmon nanocavity. However, if the nanoparticle size is too large to have an impact on the evanescent optical mode, i.e., the optical modes of the nanoparticle and the plate coupled with each other, and peak splitting occurs in the absorption spectrum, then the evanescent mode cannot be seen as the electromagnetic background, which is beyond the consideration of this work.

Note that the proposed system above is different from the traditional dimer nanostructures [17,26]. Here, the modes of the nanoparticle and plate are decoupled. The evanescent vacuum provided by the plate is the electromagnetic background for the nano-CQED system. While in dimer nanostructures, the role of the two nanoparticles is the same, namely, the coupling between one of them alone and the emitter is comparative with that of the other one alone. For example, in [26], the dipole modes of the two nanodisks coupled with each other, forming two hybrid modes (dark mode and bright mode). Then, the bright mode is taken as the cavity mode to interact with the quantum emitter.

The dielectric constant of the metal is taken from the experimental data [32]. At wavelength $\lambda = 780$ nm, when the permittivities of the medium are $\varepsilon_b = 1.5$, 2.13, 3.0, and 4.0, the real parts of the propagation constant are $\text{Re}(k_z/k_0) = 1.257$, 1.515, 1.827, and 2.151, and the evanescent depths are $L_{\text{depth}} = 438.6$, 305.4, 213.3, and 157.0 nm, respectively, as shown in Fig. 2. The real part of the propagation constant increases with the permittivity ε_b, so the evanescent depth in the medium decreases. Meanwhile, the imaginary part of the propagation constant Im (k_z/k_0) increases; thus, the propagation distance L_{sp} decreases, but a low-loss nanofiber can be added to guide photons efficiently.

The fully quantum theory is used to handle the light–matter interaction. Under the rotating wave and dipole approximations, the Hamiltonian of the nano-CQED system embedded in the EV is $H = \hbar\omega_e\sigma^\dagger\sigma + \hbar\omega_c a^\dagger a + \hbar g_0(\sigma^\dagger a + \sigma a^\dagger)$, where $\sigma^\dagger$ (σ) is the raising (lowering) operator of the emitter, and $a^\dagger$ (a) is the creation (annihilation) operator for the longitudinal mode of the Ag nanocavity. ω_e (ω_c) is the frequency of the emitter (nanocavity). The g_0 represents the coupling coefficient between the longitudinal mode of the Ag nanoparticle

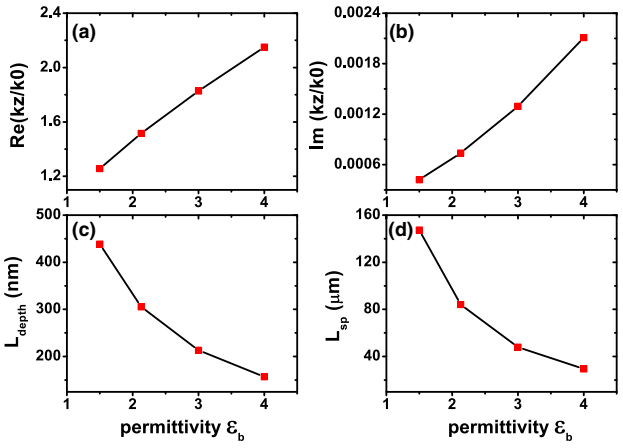

Fig. 2. Dispersion relations for evanescent electromagnetic modes of the Ag plate. (a) Real part and (b) imaginary part of the propagation constant k_z/k_0 for the evanescent modes. (c) Evanescent depth L_{depth} in the medium and (d) propagation length L_{sp} for the evanescent mode. When the permittivity increases, the evanescent depth in the medium decreases, which results in a more confined field and would be beneficial to the coupling coefficient enhancement.

and the single emitter in the EV. The master equation $\dot{\rho} = -\frac{i}{\hbar}[H,\rho] - \frac{\gamma}{2}(\sigma^{\dagger}\sigma\rho - \sigma\rho\sigma^{\dagger} + \text{H.c.}) - \frac{\kappa}{2}(a^{\dagger}a\rho - a\rho a^{\dagger} + \text{H.c.})$ governed the dynamics of the nano-CQED system, where κ is the decay rate of the nanocavity mode, and γ is for the emitter to modes other than the nanocavity mode [4]. Specifically, $\gamma = \gamma_{\text{ev}} + \gamma_{\text{rad}}$, where the γ_{ev} is the decay rate to the evanescent mode, and the γ_{rad} is that to the far field. The evanescent mode does not involve the reversible interaction process because it is the electromagnetic background of the nano-CQED system. However, compared with free vacuum, the coupling coefficients are greatly enhanced because of the exponential decay of the evanescent field.

The parameters g_0, κ, and γ in this hybrid system can be simulated by commercial COMSOL multiphysics software [9,16,33]. A spherical module with a radius of 2000 nm is set up, where the bottom hemisphere is the Ag plate and the top hemisphere is the dielectric medium. The Ag nanoparticle is located in the dielectric medium, and d represents the distance between the nanoparticle and the Ag plate. In order to minimize boundary reflections, we introduced a perfectly matched spherical layer with the thickness $\lambda/2$ outside the spherical module. A phase-matching high index material is put in one side of the Ag plate to efficiently excite the evanescent wave of the Ag plate.

The theories of calculating g_0, κ, and γ are as follows. The coupling coefficient is $g_0 = \frac{\vec{E}\cdot\vec{\mu}}{\hbar}$, which is proportional to the transition dipole moment μ of the emitter and the field $\vec{E}$ corresponding to a single excitation of the Ag nanoparticle longitudinal mode. To obtain the field $\vec{E}$, we should first subtract the background of the evanescent wave from the total electromagnetic field to obtain the longitudinal mode, then normalize its total energy to the single photon energy. The nanocavity mode damping rate κ is obtained by the FWHM of the Ag nanoparticle absorption spectrum, which is calculated by volume integration over the resistive loss in the simulation.

The emitter decay rate is $\gamma = \gamma_{\text{ev}} + \gamma_{\text{rad}} = \gamma_t - \gamma_{\text{nr}}$, where γ_t and γ_{nr} are the total decay rate and the nonradiative decay rate due to the ohmic losses, respectively. Note that we have ignored the scattering loss γ_{scat} of the nanoparticle, which is much smaller than the absorption loss γ_{nr}, for our considered small nanoparticles. A point dipole emitter is located in the nanogap between the Ag nanoparticle and the Ag plate. The energy W_t flowing out through a nanosphere enveloping the emitter is calculated. As for nonradiative energy W_{nr}, not only the absorption for the Ag nanoparticle is included, but the absorption for the charge images of the nanoparticle and the emitter in the plate is also included. Then, the decay rate γ can be derived by $\gamma/\gamma_0 = (\gamma_t - \gamma_{\text{nr}})/\gamma_0 = (W_t - W_{\text{nr}})/W_0$, where W_0 is the energy flowing out through a nanosphere enveloping the same dipole emitter in free space, and γ_0 is the decay rate of the emitter in free vacuum.

3. HIGH-DIELECTRIC CONSTANT ENHANCED COUPLING COEFFICIENTS

The EV can enhance the photon–exciton coupling [16], but the impact of the dielectric constant of the embedding medium on the coupling coefficient enhancement was not discussed. Here, we changed the permittivity ε_b of the medium above the plate. Specifically, the 2D evanescent optical field distribution for $\varepsilon_b = 4.0$ is shown in the Fig. 1(b). The period is consistent with the wavelength of the evanescent wave, which is calculated by $\lambda_{\text{ev}} = 780\ \text{nm}/\text{Re}(k_z/k_0) = 362.7\ \text{nm}$. The Ag nanoparticle is placed close to the plate, and the nanogap between them is set as $d = 1$ nm. The zero point of the y axis is at surface of the Ag plate. Owing to the collective oscillation of free electrons in the EV, the electric field distributions of the Ag nanoparticle longitudinal mode for $\varepsilon_b = 1.5$ with $D_{\text{rod}} = 20$ nm and $a_{\text{rod}} = 49.4$ nm and $\varepsilon_b = 4.0$ with $D_{\text{rod}} = 20$ nm and $a_{\text{rod}} = 9.6$ nm are shown in Figs. 1(c) and 1(d). Both the exponential decay of the evanescent wave and the gap surface plasmon [34–36] greatly contribute to the strongly localized field. Moreover, the fields are more localized for $\varepsilon_b = 4.0$ than for $\varepsilon_b = 1.5$ because of faster exponential decay of the evanescent wave, which would result in more enhanced photon–exciton coupling.

Then, we focus on the coupling coefficient enhancement caused by the high dielectric constant. The transition dipole moment of the emitter is y-axis orientated, and the value is $\mu = 0.2$ enm, which is in the range of atomic dipole moments. When the permittivity of the medium increases as 1.5, 2.13, 3.0, and 4.0, the resonance length decreases as $a_{\text{rod}} = 49.4$ nm, 32.7 nm, 19.1 nm, and 9.6 nm for the AgNR with the diameter $D_{\text{rod}} = 20$ nm, respectively. As shown in Fig. 3, the coupling coefficients of the single emitter to the AgNR with the plate decrease first and then increase, while the coupling coefficients without the plate are close. In detail, the coupling coefficients with the plate increase from 7.1, 7.6, 8.1, to 8.7 times larger than that in homogeneous vacuum. One can find that a high dielectric constant results in larger photon–exciton coupling enhancement. The main reason is that, with the permittivity ε_b increasing, the real part of the propagation constant Re

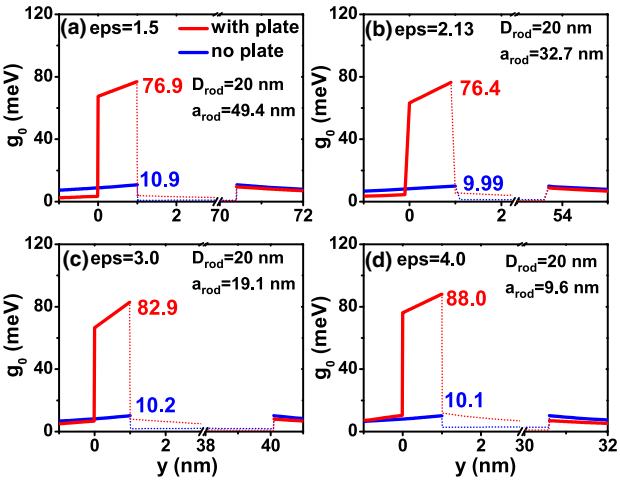

Fig. 3. Larger coupling coefficients enhancement for smaller evanescent depth. The coupling coefficients g_0 along the central axis of the AgNR for (a) $\varepsilon_b = 1.5$, $D_{\text{rod}} = 20$ nm, $a_{\text{rod}} = 49.4$ nm; (b) $\varepsilon_b = 2.13$, $D_{\text{rod}} = 20$ nm, $a_{\text{rod}} = 32.7$ nm, (c) $\varepsilon_b = 3.0$, $D_{\text{rod}} = 20$ nm, $a_{\text{rod}} = 19.1$ nm, and (d) $\varepsilon_b = 4.0$, $D_{\text{rod}} = 20$ nm, $a_{\text{rod}} = 9.6$ nm. The coupling coefficient enhancements are 7.1, 7.6, 8.1, and 8.7 times. The coupling coefficient enhancement increases with the permittivity because the faster exponential decay of the evanescent wave results in more localized plasmon mode within smaller evanescent depth.

(k_z/k_0) increases, then evanescent depth L_{depth} decreases, resulting in a more confined evanescent field owing to the faster exponential decay of the evanescent wave. Thus, a more localized plasmon mode of the nanoparticle is obtained to increase the coupling enhancement.

4. ENHANCEMENT OF THE COUPLING COEFFICIENTS VIA CHANGING OTHER PARAMETERS

This section presents the coupling coefficient enhancement at a fixed permittivity $\varepsilon_b = 2.13$ of the medium. First, the coupling coefficients enhanced via changing the size of the cylindrical nanorod are demonstrated. Then, results for a larger nanogap are clarified. Finally, large absolute values of the coupling coefficients for the Ag pyramid or bipyramid are obtained.

The enhanced coupling coefficients in EV via changing the size of the AgNR are shown in Figs. 4(a) and 4(b). The nanogap is $d = 1$ nm. We decrease the diameter of the AgNR to $D_{\text{rod}} = 14$ nm and $D_{\text{rod}} = 10$ nm, whose resonance lengths in an evanescent wave at $\lambda = 780$ nm are 27.5 and 22.0 nm, respectively. The resonance length decreases when the nanorod diameter decreases. For $D_{\text{rod}} = 14$ nm (or $D_{\text{rod}} = 10$ nm), the coupling coefficient of 84.8 meV (or 97.3 meV) at the nanogap is 5.1 (or 4.0) times larger than the value of 16.6 meV (or 24.3 meV) without a plate. By comparing these results with those in Fig. 3(b), more enhanced coupling coefficients are obtained for longer AgNRs because, within the same penetration length, the exponential decay of the evanescent wave results in a more localized plasmon mode for longer nanoparticles. The absolute values of the coupling coefficients are smaller for larger size AgNRs owing to the increased mode volume. These are in agreement with the previous work [16].

The dielectric constant of the embedding medium and the length of the AgNR can affect the coupling coefficient enhancement. In the evanescent field with the same embedding medium, larger coupling coefficient enhancement can be obtained for longer AgNRs. But, in the third section, shorter AgNR in the medium with a high dielectric constant can obtain a larger coupling coefficient enhancement than longer AgNR in a medium with a small dielectric constant. Thus, the impact of the dielectric constant on the coupling coefficient enhancement is larger than that of the length of the AgNR.

The coupling coefficient enhancement via changing the size of the nanogap is demonstrated [Figs. 4(c) and 4(d)]. When the distance is $d = 2$ nm, the enhancement of the coupling coefficient is 3.9 times for the nanorod with $D_{\text{rod}} = 20$ nm and $a_{\text{rod}} = 37.6$ nm. While for $d = 5$ nm, the enhancement is 2.0 times for the nanorod with $D_{\text{rod}} = 20$ nm and $a_{\text{rod}} = 43.6$ nm. Compare the two cases above with that in Fig. 3(b), and we can see that, for the nanorod with the same diameter, the resonance length of the nanorod decreases with the decrease of the nanogap size, while the enhancement of the coupling coefficients increases because a smaller nanogap results in a more localized field because of the exponential decay of the evanescent wave. With the present technology, the nanogap can be accurately controlled to 0.9 nm [29]. However, the nanogap size cannot decrease infinitely because the distance smaller than 0.3 nm would induce quantum effects [37].

Replacing the cylindrical nanorod with a pyramid or bipyramid will greatly increase the absolute value of the coupling coefficients, but the coupling coefficient enhancements are relatively small compared with those of the cylindrical nanorod [Figs. 4(e) and 4(f)]. Here, the gap distance is $d = 1$ nm. The slant angle of the ridge to the central axis of the nanoparticle is 20°. For the pyramid with the tip diameter $D_{\text{tip}} = 10$ nm and length $a = 30.6$ nm, the maximum of the coupling coefficient at the nanogap is up to 124.8 meV, and the enhancement is 3.6 times. While for the bipyramid with $D_{\text{tip}} = 10$ nm and the length $a = 49.0$ nm, the maximal coupling coefficient is 124.1 meV, and the enhancement is 4.9 times. Because more charges gathering at the nanotip result in a more localized field, i.e., the tip effect, a larger coupling coefficient than that for the cylindrical nanorod would realize strong coupling more easily.

5. DEMONSTRATION OF THE REVERSIBLE INTERACTION

Exchanging energy reversibly and Rabi splitting are signatures of strong coupling between a nanocavity and a single emitter [1]. The exact resonance between them is assumed. The gap distance is $d = 1$ nm. Here, we analyze two cases. First, for $\varepsilon_b = 1.5$, the damping rate of the specific plasmon nanocavity with $D_{\text{rod}} = 20$ nm and $a_{\text{rod}} = 49.4$ nm is $\kappa_1 = 78.0$ meV. Second, for $\varepsilon_b = 4.0$, the damping rate of the nanocavity with $D_{\text{rod}} = 20$ nm and $a_{\text{rod}} = 9.6$ nm is $\kappa_2 = 64.5$ meV, while the coupling coefficient g_0^{mid} and the emitter's decay rate γ

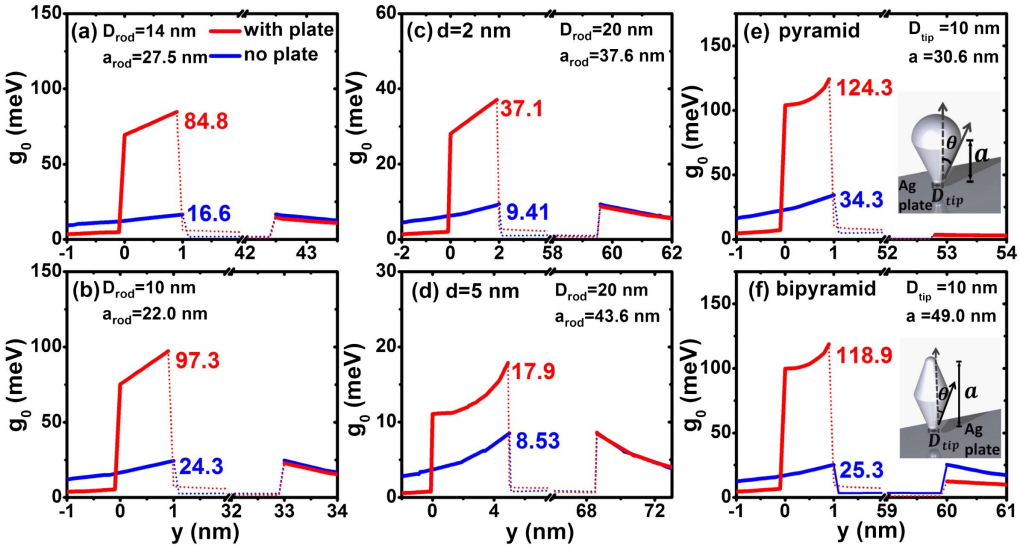

Fig. 4. Coupling coefficient enhancement via changing the radius of the AgNR, size of the nanogap, and the shape of the Ag nanoparticle. The dipole moment of the emitter is $\mu = 0.2$ enm, and the permittivity is $\varepsilon_b = 2.13$. The gap distance is $d = 1$ nm for (a), (b), (e), and (f). The coupling coefficients g_0 along the central axis of the AgNR for (a) $D_{\rm rod} = 14$ nm, $a_{\rm rod} = 27.5$ nm, and (b) $D_{\rm rod} = 10$ nm, $a_{\rm rod} = 22.0$ nm. Because the exponential decay of the evanescent wave results in a more localized plasmon mode for longer nanorods within the same penetration length, the coupling coefficients for longer AgNR increase more than that of the shorter one. The coupling coefficients g_0 for (c) $d = 2$ nm with $D_{\rm rod} = 20$ nm, $a_{\rm rod} = 37.6$ nm, and (d) $d = 5$ nm with $D_{\rm rod} = 20$ nm, $a_{\rm rod} = 43.6$ nm. With the decrease in the size of the nanogap, the enhancement of the coupling coefficients increases because smaller nanogap results in a more localized field owing to the exponential decay of the evanescent wave. Coupling coefficients for (e) the Ag pyramid with $D_{\rm tip} = 10$ nm, $a = 30.6$ nm and (f) the Ag bipyramid with $D_{\rm tip} = 10$ nm, $a = 49.0$ nm. The slant angle of the ridge to the central axis of the nanoparticle is 20°. The larger coupling coefficient is mainly due to the strongly localized field close to the nanotip.

at the center of the nanogap are proportional to the transition dipole moment μ and square of μ, respectively [38,39].

With the above-mentioned parameters $g_0^{\rm mid}$, κ, and γ simulated by the commercial COMSOL software, the dynamical evolution and fluorescence spectra of the nano-CQED systems are calculated using the Python toolbox [40]. The excited-state probability of the emitter is $\rho_{ee} = \langle \sigma^\dagger \sigma \rangle$, and the average number of photons in the nanocavity is $\rho_{nn} = \langle a^\dagger a \rangle$. When calculating the dynamic evolution of ρ_{ee} and ρ_{nn}, the emitter is in the excited state, and there are no photons in the nanocavity initially, i.e., $\rho_{ee}(t = 0) = 1$ and $\rho_{nn}(t = 0) = 0$. It is not necessary to add any driving field; thus, the quantum emitter interacts with the quantized vacuum state $|0\rangle$. Then, when calculating the fluorescence of the steady state, we add a thermal reservoir to drive the nanocavity mode. The reservoir reduced density operator ρ_R is the multimode extension of the thermal operator, i.e., $\rho_R = \prod_k [1 - e^{-\frac{\hbar\omega_k}{k_B T}}] e^{-\frac{\hbar\omega_k b_k^\dagger b_k}{k_B T}}$, where k_B is the Boltzmann constant and T is the temperature. The fluorescence spectrum is the Fourier-transformed electric field operator $\langle E^-(\vec{r}, t) E^+(\vec{r}, t + \tau) \rangle \propto \sigma^\dagger(t) \sigma(t + \tau)$, which can be written as $S(\vec{r}, \omega) = \frac{1}{\pi} {\rm Re} \int {\rm d}\tau \langle E^-(\vec{r}, t) E^+(\vec{r}, t + \tau) \rangle e^{i\omega t}$.

The processes of exchanging energy for $\varepsilon_b = 1.5$ are displayed in Figs. 5(a) and 5(b). When $\mu = 0.08$ enm, the decrease in ρ_{ee} and increase in ρ_{nn} simultaneously indicate that the emitter and the nanocavity start exchanging energy, which is accompanied with tiny Rabi splitting in the fluorescence spectra, as shown in Fig. 5(c). By increasing the dipole moment to $\mu = 0.20$ enm, the increased coupling coefficients $g_0^{\rm mid}$ lead to faster energy exchanging because the frequency of the exchanging energy is $2g_0^{\rm mid}$. The decreases in the peak values of ρ_{ee} and ρ_{nn} are due to the damping rates of the emitter and nanocavity

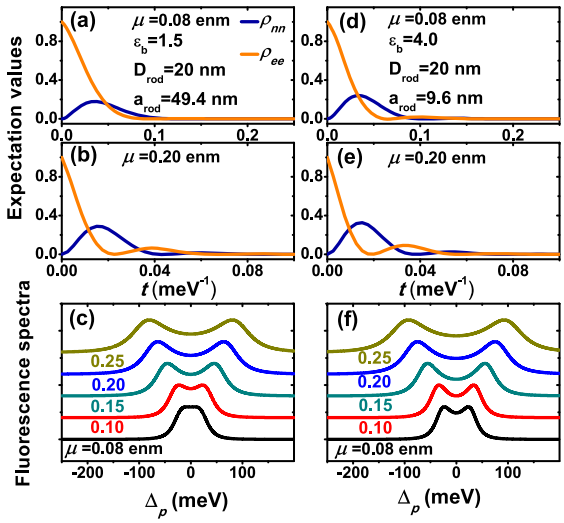

Fig. 5. Reversible interaction and Rabi splitting in EV. The permittivity $\varepsilon_b = 1.5$, $D_{\rm rod} = 20$ nm, and $a_{\rm rod} = 49.4$ nm for (a), (b), and (c). While for (d), (e), and (f), $\varepsilon_b = 4.0$, $D_{\rm rod} = 20$ nm, and $a_{\rm rod} = 9.6$ nm. (a), (b), (d), and (e) Population probabilities ρ_{nn} in the AgNR nanocavity and ρ_{ee} in the excited state of the emitter for $\mu = 0.08$ enm and 0.20 enm. (c) and (f) Fluorescence spectra versus the probe field detuning $\Delta_p = \omega - \omega_e$ for various dipole moments of the emitter.

mode. The emitter exchanged energy several times with the nanocavity before it decayed to the ground state, which is the characteristic of strong coupling. The fluorescence spectra show that larger Rabi splitting appears for a larger dipole moment because the fluorescence intensity reaches maximum at the positions $\pm g_0^{\mathrm{mid}}$, which is consistent with that of the dressed state analysis [41]. The results for $\varepsilon_b = 4.0$ are shown in Figs. 5(d)–5(f). Compared with that for $\varepsilon_b = 1.5$, faster energy exchanging and larger Rabi splitting can be obtained for the same dipole moment owing to larger coupling coefficient g_0^{mid}.

It is known that the typical value of atomic dipole moments is $\mu = 0.05 \sim 0.25$ enm. However, for the Rydberg atom with a large electron orbital, it is 0.5 enm [42], which is larger than that of normal atoms. As for quantum dots and the micromolecular, it is generally larger than 0.5 enm [17,43,44]. Therefore, for the emitters noted above, the experimental realization of the aforementioned Rabi splitting is possible in 2D EV.

6. DISCUSSION AND SUMMARY

Metallic plates and nanoparticles may be controllably fabricated with the development of experimental technology, such as electron beam evaporation, electron beam lithography, and focused ion beam lithography [29,45–47]. The permittivity $\varepsilon_b = 2.13$ is corresponding to the doped silica [21], which can also be replaced by some other medium with refractive index from 1.0 to 1.8 [29]. Through layer-by-layer polyelectrolyte film or the cladding molecular spacers, the nanogap between them can be accurately controlled [29,36,48,49]. In a spin-coated ultrathin crystalline film of p-terphenyl, terrylene molecules can be successfully aligned [50], and proper orientation of the emitter can be made using the host–guest chemistry of macrocyclic cucurbit[n]uril molecules [29], which makes it possible to insert a single upright emitter in the nanogap. Through the microscope objective, the total internal reflection of the *p*-polarized incident light can excite the emitter [51]. Thus, the greatly enhanced photon–exciton coupling in a nano-CQED system could be experimentally realized in the near feature.

In summary, we theoretically studied high-dielectric constant enhanced photon–exciton coupling in a nano-CQED system embedded in 2D EV. When the dielectric constant increases, the evanescent depth decreases; thus, a more confined evanescent field leads to larger coupling coefficient enhancement. Further enhanced photon–exciton coupling is investigated by changing the size of the Ag nanoparticle, size of the gap distance, and shape of the nanoparticle. Based on strong photon–exciton coupling, the setup of the nano-CQED system could be used as a quantum node. Owing to the broad 2D evanescent field region, multi-nano-CQED systems can be placed in the same evanescent vacuum, which has potential applications in scalable quantum networks [4,52]. Such exciton–polariton in a nanocavity is promising for emerging technological applications and exploring polaritons for quantum computation and simulation [53]. Moreover, the reversible interaction, entanglement, and state manipulation are promising to be realized in this nano-CQED system, which will have an important impact on on-chip quantum information processing.

Funding. National Key R&D Program of China (2018YFB1107200); National Natural Science Foundation of China (NSFC) (11525414, 11734001).

REFERENCES

1. K. J. Vahala, "Optical microcavities," Nature **424**, 839–846 (2003).
2. P. Zoller, Th. Beth, D. Binosi, R. Blatt, H. Briegel, D. Bruss, T. Calarco, J. I. Cirac, D. Deutsch, J. Eisert, A. Ekert, C. Fabre, N. Gisin, P. Grangiere, M. Grass, S. Haroche, A. Imamoglu, A. Karlson, J. Kempe, L. Kouwenhoven, S. Kröll, G. Leuchs, M. Lewenstein, D. Loss, N. Lütkenhaus, S. Massar, J. E. Mooij, M. B. Plenio, E. Polzik, S. Popescu, G. Rempe, A. Sergienko, D. Suter, J. Twamley, G. Wendin, R. Werner, A. Winter, J. Wrachtrup, and A. Zeilinger, "Quantum information processing and communication," Eur. Phys. J. D **36**, 203–228 (2005).
3. H. Walther, B. T. H. Varcoe, B.-G. Englert, and T. Becker, "Cavity quantum electrodynamics," Rep. Prog. Phys. **69**, 1325–1382 (2006).
4. H. J. Kimble, "The quantum internet," Nature **453**, 1023–1030 (2008).
5. M. S. Tame, K. R. McEnery, S. K. Özdemir, J. Lee, S. A. Maier, and M. S. Kim, "Quantum plasmonics," Nat. Phys. **9**, 329–340 (2013).
6. Z. Jacob and V. M. Shalaev, "Plasmonics goes quantum," Science **334**, 463–464 (2011).
7. A. V. Akimov, A. Mukherjee, C. L. Yu, D. E. Chang, A. S. Zibrov, P. R. Hemmer, H. Park, and M. D. Lukin, "Generation of single optical plasmons in metallic nanowires coupled to quantum dots," Nature **450**, 402–406 (2007).
8. D. E. Chang, A. S. Sørensen, P. R. Hemmer, and M. D. Lukin, "Quantum optics with surface plasmons," Phys. Rev. Lett. **97**, 053002 (2006).
9. H. Lian, Y. Gu, J. Ren, F. Zhang, L. Wang, and Q. Gong, "Efficient single photon emission and collection based on excitation of gap surface plasmon," Phys. Rev. Lett. **114**, 193002 (2015).
10. M. K. Dezfouli and S. Hughes, "Quantum optics model of surface-enhanced Raman spectroscopy for arbitrarily shaped plasmonic resonators," ACS Photon. **4**, 1245–1256 (2017).
11. M. I. Stockman, "Nanoplasmonics: past, present, and glimpse into future," Opt. Express **19**, 22029–22106 (2011).
12. P. Bharadwaj, B. Deutsch, and L. Novotny, "Optical antennas," Adv. Opt. Photon. **1**, 438–483 (2009).
13. K. Okamoto, S. Vyawahare, and A. Scherer, "Surface-plasmon enhanced bright emission from CdSe quantum-dot nanocrystals," J. Opt. Soc. Am. B **23**, 1674–1678 (2006).
14. S. Zanotto, F. P. Mezzapesa, F. Bianco, G. Biasiol, L. Baldacci, M. S. Vitiello, L. Sorba, R. Colombelli, and A. Tredicucci, "Perfect energy-feeding into strongly coupled systems and interferometric control of polariton absorption," Nat. Phys. **10**, 830–834 (2014).
15. M. Sukharev and A. Nitzan, "Optics of exciton-plasmon nanomaterials," J. Phys. Condens. Matter **29**, 443003 (2017).
16. J. Ren, Y. Gu, D. Zhao, F. Zhang, T. Zhang, and Q. Gong, "Evanescent-vacuum-enhanced photon-exciton coupling and fluorescence collection," Phys. Rev. Lett. **118**, 073604 (2017).
17. S. Savasta, R. Saija, A. Ridolfo, O. D. Stefano, P. Denti, and F. Borghese, "Nanopolaritons: vacuum Rabi splitting with a single quantum dot in the center of a dimer nanoantenna," ACS Nano **4**, 6369–6376 (2010).
18. A. Salomon, R. J. Gordon, Y. Prior, T. Seideman, and M. Sukharev, "Strong coupling between molecular excited states and surface plasmon modes of a slit array in a thin metal film," Phys. Rev. Lett. **109**, 073002 (2012).
19. E. Waks and D. Sridharan, "Cavity QED treatment of interactions between a metal nanoparticle and a dipole emitter," Phys. Rev. A **82**, 043845 (2010).
20. J. Yang, M. Perrin, and P. Lalanne, "Analytical formalism for the interaction of two-level quantum systems with metal nanoresonators," Phys. Rev. X **5**, 021008 (2015).

21. A. Delga, J. Feist, J. Bravo-Abad, and F. J. Garcia-Vidal, "Quantum emitters near a metal nanoparticle: strong coupling and quenching," Phys. Rev. Lett. **112**, 253601 (2014).
22. P. Törmä and W. L. Barnes, "Strong coupling between surface plasmon polaritons and emitters: a review," Rep. Prog. Phys. **78**, 013901 (2015).
23. J. Bellessa, C. Bonnand, and J. C. Plenet, "Strong coupling between surface plasmons and excitons in an organic semiconductor," Phys. Rev. Lett. **93**, 036404 (2004).
24. T. K. Hakala, J. J. Toppari, A. Kuzyk, M. Pettersson, H. Tikkanen, H. Kunttu, and P. Törmä, "Vacuum Rabi splitting and strong-coupling dynamics for surface-plasmon polaritons and Rhodamine 6G molecules," Phys. Rev. Lett. **103**, 053602 (2009).
25. D. E. Gómez, K. C. Vernon, P. Mulvaney, and T. J. Davis, "Surface plasmon mediated strong exciton-photon coupling in semiconductor nanocrystals," Nano Lett. **10**, 274–278 (2010).
26. A. E. Schlather, N. Large, A. S. Urban, P. Nordlander, and N. J. Halas, "Near-field mediated plexcitonic coupling and giant Rabi splitting in individual metallic dimers," Nano Lett. **13**, 3281–3286 (2013).
27. G. Zengin, M. Wersäll, S. Nilsson, T. J. Antosiewicz, M. Käll, and T. Shegai, "Realizing strong light-matter interactions between single-nanoparticle plasmons and molecular excitons at ambient conditions," Phys. Rev. Lett. **114**, 157401 (2015).
28. R. Liu, Z.-K. Zhou, Y.-C. Yu, T. Zhang, H. Wang, G. Liu, Y. Wei, H. Chen, and X.-H. Wang, "Strong light-matter interactions in single open plasmonic nanocavities at the quantum optics limit," Phys. Rev. Lett. **118**, 237401 (2017).
29. R. Chikkaraddy, B. de Nijs, F. Benz, S. J. Barrow, O. A. Scherman, E. Rosta, A. Demetriadou, P. Fox, O. Hess, and J. J. Baumberg, "Single-molecule strong coupling at room temperature in plasmonic nanocavities," Nature **535**, 127–130 (2016).
30. H. Groß, J. M. Hamm, T. Tufarelli, O. Hess, and B. Hecht, "Near-field strong coupling of single quantum dots," Sci. Adv. **4**, eaar4906 (2018).
31. H. Raether, *Surface Plasmons on Smooth and Rough Surfaces and on Gratings* (Springer-Verlag, 1986).
32. P. B. Johnson and R. W. Christy, "Optical constants of noble metals," Phys. Rev. B **6**, 4370–4379 (1972).
33. X. Shan, I. Dez-Pérez, L. Wang, P. Wiktor, Y. Gu, L. Zhang, W. Wang, J. Lu, S. Wang, Q. Gong, J. Li, and N. Tao, "Imaging the electrocatalytic activity of single nanoparticles," Nat. Nanotechnol. **7**, 668–672 (2012).
34. F. Le, N. Z. Lwin, J. M. Steele, M. Käll, N. J. Halas, and P. Nordlander, "Plasmons in the metallic nanoparticle-film system as a tunable impurity problem," Nano Lett. **5**, 2009–2013 (2005).
35. J. J. Mock, R. T. Hill, A. Degiron, S. Zauscher, A. Chilkoti, and D. R. Smith, "Distance-dependent plasmon resonant coupling between a gold nanoparticle and gold film," Nano Lett. **8**, 2245–2252 (2008).
36. J. B. Lassiter, F. McGuire, J. J. Mock, C. Cirac, R. T. Hill, B. J. Wiley, A. Chilkoti, and D. R. Smith, "Plasmonic waveguide modes of film-coupled metallic nanocubes," Nano Lett. **13**, 5866–5872 (2013).
37. K. J. Savage, M. M. Hawkeye, R. Esteban, A. G. Borisovand, J. Aizpurua, and J. J. Baumberg, "Revealing the quantum regime in tunnelling plasmonics," Nature **491**, 574–577 (2012).
38. K. Słowik, R. Filter, J. Straubel, F. Lederer, and C. Rockstuhl, "Strong coupling of optical nanoantennas and atomic systems," Phys. Rev. B **88**, 195414 (2013).
39. M. O. Scully and M. S. Zubairy, *Quantum Optics* (Cambridge University, 1997).
40. J. R. Johansson, P. D. Nation, and F. Nori, "QuTiP 2: A Python framework for the dynamics of open quantum systems," Comput. Phys. Commun. **184**, 1234–1240 (2013).
41. C. Cohen-Tannoudji and S. Reynaud, "Dressed-atom description of resonance fluorescence and absorption spectra of a multi-level atom in an intense laser beam," J. Phys. B **10**, 345–363 (1977).
42. M. Saffman, T. G. Walker, and K. Mølmer, "Quantum information with Rydberg atoms," Rev. Mod. Phys. **82**, 2313–2363 (2010).
43. W. Wang, P. Vasa, R. Pomraenke, R. Vogelgesang, A. D. Sio, E. Sommer, M. Maiuri, C. Manzoni, G. Cerullo, and C. Lienau, "Interplay between strong coupling and radiative damping of excitons and surface plasmon polaritons in hybrid nanostructures," ACS Nano **8**, 1056–1064 (2014).
44. P. Vasa, W. Wang, R. Pomraenke, M. Lammers, M. Maiuri, C. Manzoni, G. Cerullo, and C. Lienau, "Real-time observation of ultrafast Rabi oscillations between excitons and plasmons in metal nanostructures with J-aggregates," Nat. Photonics **7**, 128–132 (2013).
45. B. J. Wiley, Y. Chen, J. M. McLellan, Y. Xiong, Z.-Y. Li, D. Ginger, and Y. Xia, "Synthesis and optical properties of silver nanobars and nanorice," Nano Lett. **7**, 1032–1036 (2007).
46. T. Zhang, H. Shen, G. Lu, J. Liu, Y. He, Y. Wang, and Q. Gong, "Single bipyramid plasmonic antenna orientation determined by direct photoluminescence pattern imaging," Adv. Opt. Mater. **1**, 335–342 (2013).
47. J. Qi, Y. Xiang, W. Yan, M. Li, L. Yang, Z. Chen, W. Cai, J. Chen, Y. Li, Q. Wu, X. Yu, Q. Sun, and J. Xu, "Excitation of the tunable longitudinal higher-order multipole SPR modes by strong coupling in large-area metal sub-10 nm-gap array structures and its application," J. Phys. Chem. C **120**, 24932–24940 (2016).
48. G. M. Akselrod, C. Argyropoulos, T. B. Hoang, C. Cirac, C. Fang, J. Huang, D. R. Smith, and M. H. Mikkelsen, "Probing the mechanisms of large Purcell enhancement in plasmonic nanoantennas," Nat. Photonics **8**, 835–840 (2014).
49. D. O. Sigle, J. T. Hugall, S. Ithurria, B. Dubertret, and J. J. Baumberg, "Probing confined phonon modes in individual CdSe nanoplatelets using surface-enhanced Raman scattering," Phys. Rev. Lett. **113**, 087402 (2014).
50. R. J. Pfab, J. Zimmermann, C. Hettich, I. Gerhardt, A. Renn, and V. Sandoghdar, "Aligned terrylene molecules in a spin-coated ultrathin crystalline film of p-terphenyl," Chem. Phys. Lett. **387**, 490–495 (2004).
51. K. G. Lee, X. W. Chen, H. Eghlidi, P. Kukura, R. Lettow, A. Renn, V. Sandoghdar, and S. Götzinger, "A planar dielectric antenna for directional single-photon emission and near unity collection efficiency," Nat. Photonics **5**, 166–169 (2011).
52. A. Tomadin and R. Fazio, "Many-body phenomena in QED-cavity arrays," J. Opt. Soc. Am. B **27**, A130–A136 (2010).
53. D. Sanvitto and S. Kéna-Cohen, "The road towards polaritonic devices," Nat. Mater. **15**, 1061–1073 (2016).